IAEA nuclear fusion

PAPER • OPEN ACCESS

Impact of toroidal magnetic field direction on integrated ELM-stable operation and divertor power exhaust via boron powder injection in EAST

To cite this article: Zhen Sun *et al* 2026 *Nucl. Fusion* **66** 036028

View the article online for updates and enhancements.

You may also like

- Systematic multi-machine analysis of the exhaust time-dependent behavior in tokamaks
M. van Berkel, G.L. Derks, L. Ceelen et al.

- Optimised ‘hybrid’ scenario H-mode plasmas for W radiation control in JET with the Be/W wall
A.R. Field, C. Angioni, I.S. Carvalho et al.

- Stabilization and re-excitation of sawtooth oscillations due to energetic particles in tokamaks
H.X. Zhang, H.W. Zhang, Z.W. Ma et al.

This content was downloaded from IP address 73.101.109.153 on 26/02/2026 at 15:41

OPEN ACCESS
IOP Publishing | International Atomic Energy Agency
Nuclear Fusion
Nucl. Fusion 66 (2026) 036028 (18pp)
https://doi.org/10.1088/1741-4326/ae3fac

Impact of toroidal magnetic field direction on integrated ELM-stable operation and divertor power exhaust via boron powder injection in EAST

Zhen Sun[1,*], Rajesh Maingi[1], Lei Peng[3,*], Xin Lin[2], Wei Xu[2], Zhe Wang[2], Qingquan Yang[2], Genfan Ding[2], Fang Ding[2], Kaifu Gan[5], Ahmed Diallo[1], Kevin Tritz[4], Tianfu Zhou[2], Yifeng Wang[2], Liang Chen[2], Kaixuan Ye[2], Wei Wang[2], Yunxin Cheng[2], Lingyi Meng[2], Yifei Jin[2], Ling Zhang[2], Yanmin Duan[2], Jizhong Sun[6], Alexander Nagy[1], Alessandro Bortolon[1], Guizhong Zuo[2,*], Jinping Qian[2], Xianzu Gong[2], Jiansheng Hu[2] and the EAST Team[a]

[1] Princeton Plasma Physics Laboratory, Princeton, NJ 08540, United States of America
[2] Institute of Plasma Physics, Chinese Academy of Sciences, Hefei, Anhui 230031, China
[3] Henan University of Engineering, Zhengzhou, Henan 451191, China
[4] Johns Hopkins University, Baltimore MD 21211, United States of America
[5] University of Tennessee, Knoxville, TN 37996, United States of America
[6] Dalian University of Technology, Dalian, Liaoning 116024, China

E-mail: leipeng@haue.edu.cn, zuoguizh@ipp.ac.cn and zsun@pppl.gov

Received 6 August 2025, revised 22 December 2025
Accepted for publication 30 January 2026
Published 13 February 2026

Abstract

We report the first in-depth comparison of the impact of toroidal magnetic field direction on solid boron injection used for Edge-Localized Mode (ELM) control, power exhaust, and core high-Z impurity control in the Experimental Advanced Superconducting Tokamak. With favorable ion ∇B drift towards the upper X-point in an upper-single-null configuration, boron injection effectively suppresses ELMs, produces a detachment of the inner divertor target, and leads to improved energy confinement. ELM suppression in this configuration is accompanied by the excitation of an Edge Harmonic Mode. In contrast, with unfavorable ion ∇B drift away from the upper X-point, boron injection also suppresses ELMs but leads to a more symmetric detachment state of both the inner and outer divertor targets, while plasma energy confinement is slightly degraded despite similar boron injection levels; a different low-frequency coherent mode without multiple harmonics is observed. Measurements from toroidally separated views show that the divertor response to boron injection is essentially toroidally symmetric, supporting the use of two-dimensional SOLPS-ITER modeling with a toroidally uniform impurity source.

[a] See Gong *et al* 2024 (https://doi.org/10.1088/1741-4326/ad4270) for the EAST Team.
[*] Authors to whom any correspondence should be addressed.

Original content from this work may be used under the terms of the Creative Commons Attribution 4.0 licence. Any further distribution of this work must maintain attribution to the author(s) and the title of the work, journal citation and DOI.

 © 2026 The Author(s). Published by IOP Publishing Ltd on behalf of the IAEA

These experimental observations are qualitatively consistent with SOLPS-ITER simulations, which highlight the critical role of $E \times B$ drift effects in setting the *Bt*-dependent in–out asymmetry of detachment and in asymmetrically transporting particles and injected impurities within the scrape-off layer and private-flux region. These findings underscore the importance of drift physics and real-time wall conditioning in controlling low-*Z* impurity transport and optimizing edge solutions for integrated, ELM-stable, high-performance tokamak operation.

Keywords: boron powder injection, ELM suppression, divertor detachment, $E \times B$ drift, core edge integration

(Some figures may appear in colour only in the online journal)

1. Introduction

Future magnetic confinement fusion reactors, such as ITER, aim to operate in sustained high-performance H-mode regimes to achieve sufficient energy gain. However, these regimes are typically plagued by transient heat and particle bursts known as Edge-Localized Modes (ELMs), which can cause severe erosion and damage to Plasma-Facing Components (PFCs), particularly the divertor targets [1–4]. Simultaneously, high steady-state heat flux to the divertor targets is a major design and operational challenge. Achieving efficient power exhaust, often through divertor detachment, is crucial for reducing the thermal load on divertor materials, especially tungsten, which is planned for use in ITER and several present-day devices due to its high melting point and sputtering resistance [5, 6].

Impurity seeding into the plasma edge or divertor is a well-established technique for mitigating ELMs and enhancing radiative power exhaust [7–12]. Low-*Z* impurities like nitrogen and neon are often preferred due to their lower core contamination risk and effective radiation in the edge [6]. Boron, in particular, has the additional benefit of providing wall conditioning by reducing recycling and gettering impurities like oxygen, leading to improved plasma performance [13–18]. Boron also has favorable radiative properties at relatively low electron temperatures (1–10 eV), typical of detached divertor conditions [19, 20]. While gas puffing is a common seeding method, injecting impurities in solid powder offers advantages, such as precise control of the injection rate, deeper penetration into the plasma, and localized deposition [19, 21–23]. Boron powder injection has been explored in several tokamaks for ELM mitigation and wall conditioning [19, 24–27].

The magnetic configuration, including the toroidal field direction and resulting $E \times B$, diamagnetic, and ∇B plasma drifts, plays a critical and multifaceted role in particle and impurity transport in the tokamak edge, particularly in the Scrape-Off Layer (SOL) and Private Flux Region (PFR) [6, 28]. These drift effects can lead to significant in–out asymmetries in plasma profiles, heat flux distribution, and impurity accumulation [29–34]. Consequently, the effectiveness and characteristics of impurity seeding for divertor detachment and ELM control are expected to be sensitive to the toroidal field direction. While the favorable *Bt* direction is often standard due to its lower H-mode power threshold, there are compelling reasons to study and understand the unfavorable *Bt* configuration, as it is essential for accessing some of the most promising alternative operational regimes. For example, I-mode operation in high-magnetic-field devices recognizes the potential advantages of the unfavorable *Bt* configuration for reactor-relevant conditions. The unfavorable direction often is beneficial for the I-mode and negative triangularity operational regime, which offers H-mode-like energy confinement without a strong density or pressure pedestal, potentially providing a natural solution for ELM mitigation and impurity exhaust [35, 36]. Furthermore, understanding plasma behavior in both *Bt* directions is crucial for validating transport and turbulence models, as the ability to predict performance across different drift configurations is a stringent test for these codes.

While some studies have investigated the effect of *Bt* direction on detachment or ELMs separately [2–4, 12, 37, 38], a comprehensive investigation of its impact on the *integrated* outcome of powder injection or gas impurity seeding, including detachment asymmetry, confinement, and associated ELM activity under both favorable and unfavorable ion ∇B drift configurations, has not been previously reported. Achieving integrated operation—simultaneously suppressing ELMs, ensuring adequate power exhaust (detachment), and preserving core confinement—with impurity injection is a complex task that depends on various plasma parameters, injection parameters (location, rate), and underlying transport physics [39]. This paper directly addresses this gap by presenting a systematic comparison, providing critical insights for optimizing integrated plasma control strategies.

The Experimental Advanced Superconducting Tokamak (EAST) is a superconducting tokamak with an ITER-like tungsten divertor and heating systems, designed for long-pulse, high-performance operation [40]. EAST has recently achieved significant progress towards integrated steady-state scenarios. This makes EAST an ideal platform to study the interplay between impurity injection, edge transport, and integrated plasma control strategies relevant to ITER.

This paper presents the results of experiments on EAST investigating the impact of toroidal field direction on ELM-stable operation and divertor power exhaust achieved through boron powder injection. We find that the *Bt* direction significantly alters the divertor detachment behavior, plasma confinement, and the characteristics of edge turbulence activity associated with ELM suppression. We interpret these findings in the context of $E \times B$ drift physics, supported by SOLPS-ITER simulations and experimental measurements of impurity distribution. The remainder of the paper is structured as follows:

section 2 describes the experimental setup, including the boron powder injection system and relevant diagnostics. Section 3 presents the experimental results for both favorable and unfavorable *Bt* directions, including detailed time traces, divertor measurements, ELM activity, analysis of boron injection rate scans, and a qualitative comparison with SOLPS-ITER simulations. Section 4 discusses the implications of these findings for integrated scenario development and concludes the paper.

2. Experimental and modeling setup

EAST is a medium-sized superconducting tokamak with a major radius $R = 1.85$ m and a minor radius $a = 0.5$ m. It is equipped with actively water-cooled tungsten monoblock PFCs, including an ITER-like tungsten divertor, capable of handling high heat loads during long pulses. EAST has a flexible heating system that combines Neutral Beam Injection (NBI), radio-frequency heating, including Lower Hybrid Wave (LHW), Ion Cyclotron Resonance Heating (ICRH), and Electron Cyclotron Resonant Heating (ECH). These capabilities enable the study of high-performance H-mode plasmas with durations extending up to 1000 s in I-mode and over 400 s in H-mode [41]. While the divertor targets consist of tungsten (W) monoblocks, the first wall of the main chamber is composed of molybdenum (Mo) tiles. Consequently, Mo emission serves as a proxy for impurity influx from the main chamber wall, distinct from the divertor tungsten source.

Boron powder was injected into the EAST plasma using an Impurity Powder Dropper (IPD), developed in Princeton Plasma Physics Laboratory [42]. The IPD allows for reproducible injection of solid powder into the plasma edge. The system utilizes a vertically mounted piezoelectric crystal, driven by an adjustable voltage, to vibrate a surface and horizontally feed powder into a vertical drop tube. The powder then falls gravitationally into the tokamak vacuum vessel. For the experiments described here, boron powder with a nominal size of ∼70 μm and a purity exceeding 99.99% from Alfa Aesar Corporation was used. The powder flow rate could be adjusted over a range of 2–250 mg s^{-1}. The IPD system incorporates an optical flowmeter that provides a real-time measurement of the powder mass flow rate. This is cross-calibrated with the voltage applied to the piezoelectric crystal. In the flowmeter, a collimated beam of light intersects the powder drop trajectory through a gap, and the relative attenuation of the transmitted light by the falling powder is taken as a measurement of the powder rate.

The injection location was strategically chosen to deliver the powder into the PFR just above the upper X-point during upper single-null (USN) operation. A vertical guide tube with a radial position of $R = 1.57$ m directed the falling powder. As indicated by the red arrow in figure 1, the powder trajectory is assumed to be primarily gravitational, accelerating to approximately 9 m s^{-1} by the time it reaches the vicinity of the X-point, located about 4.5 m below the piezoelectric crystals. The precise interaction location and particle ablation physics are complex but are expected to occur near the separatrix region above the X-point.

A suite of diagnostics was employed to monitor the plasma response to boron injection, as illustrated in figure 1. The poloidal layout shows the approximate locations and viewing chords of key measurements relative to the plasma equilibrium for four representative discharges (#85041, #85043, #93468, and #93469). Two flat-field grazing incidence extreme ultraviolet (EUV) spectrometers (covering 1–13 nm and 2–50 nm) with fast-time response and 5 ms resolution monitored the intensity of highly-ionized impurity emission. Specifically, *B–V* with a transition of 1s–3p ($\lambda = 4.098$ nm, ionization energy ∼ 340 eV) is utilized for monitoring B powder injection. The core W spectra were analyzed using an unresolved transition array (W-UTA) monitoring highly-ionized W ions in several stages of ionization (e.g. W27+–W45+, 4.5–7 nm) [43]. A 64-channel bolometer (absolute extreme ultraviolet photodiodes, AXUV) diagnostic is used to measure plasma radiation and is also sensitive to low-frequency oscillation phenomena [44]. Magnetic fluctuation is monitored by four arrays of Mirnov probes (MPs) mounted on the vacuum wall. A filter-scope spectral diagnosis measures the Dα emission intensity. The ion saturation current and electron temperature on the divertor target plates are measured by divertor triple Langmuir probes (LPs). A total of 54 triple divertor LPs are distributed on the inner and outer upper divertor target plates, with the spatial and temporal resolutions of 12–18 mm poloidally and 20 μs, respectively [45]. To assess the toroidal symmetry of the plasma response, key diagnostics were configured to view the same upper divertor region poloidally but at widely separated toroidal angles. Two identical upper divertor LP arrays are installed at the same poloidal locations on the inner and outer targets but are separated by 135° toroidally (Ports D and O). Additionally, the visible spectrometer viewing the upper outer target and the EUV spectrometer viewing the midplane are located approximately 180° apart toroidally. Note that, because the probe tips can be transiently overheated, the absolute accuracy of the divertor triple-Langmuir-probe diagnostics is limited to roughly ±20%. During analysis, probe data showing characteristics of strong thermionic emission (e.g. a collapsed floating potential or virtual current offsets due to transient overheating) are rigorously identified and excluded from the dataset. A multichannel visible spectroscopy viewing on the outer target is dedicated to monitoring the neutrals and low ionized impurities [46].

To interpret the physical mechanisms governing the observed detachment asymmetry and impurity transport, numerical simulations were performed using the SOLPS-ITER code suite [21, 47]. The simulation grids were constructed based on the experimental magnetic equilibrium of the favorable *Bt* discharge #85043. Radial transport coefficients were determined by benchmarking the simulation against experimental upstream profiles (density and temperature) during the pre-injection phase [47]. To simulate the real-time wall conditioning and pumping effect of the deposited boron layers,

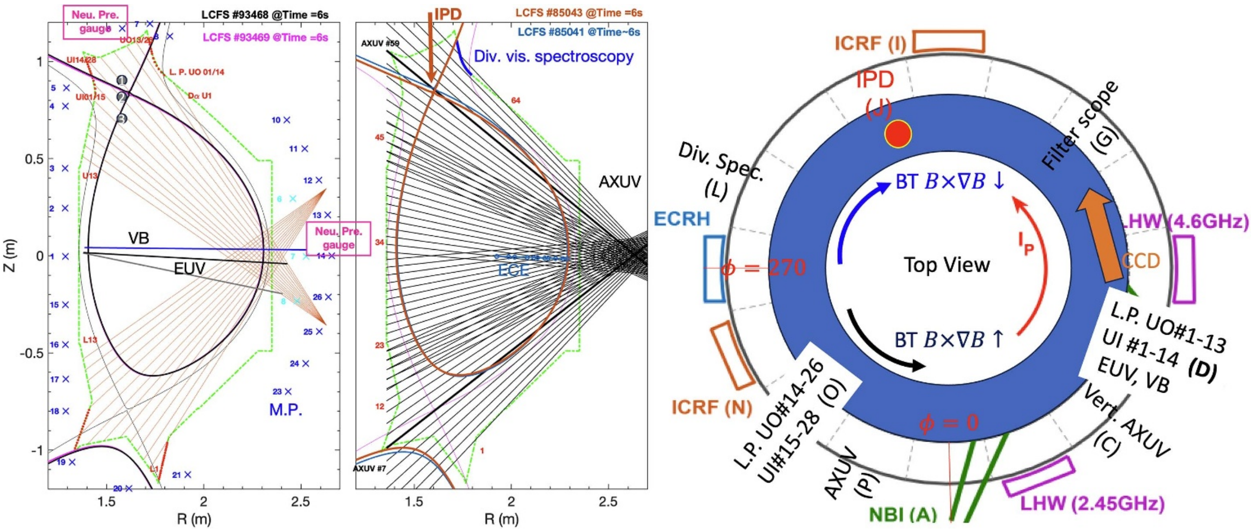

Figure 1. Poloidal and toroidal layouts of IPD and the primary diagnostics used in this study. (Left & middle) Reconstructed equilibria for favorable *Bt* (#85041 & #85043) and unfavorable *Bt* (#93468 & #93469) discharges at $t = 6$ s. The panels show the poloidal locations of the divertor LP, upper & lower D α arrays, EUV spectrometer sightlines, Mirnov probes (MPs), and neutral pressure gauges. The middle panel details sightlines for the 64-channel AXUV bolometer array, ECE radiometer, and divertor visible spectroscopy. The orange vertical arrow indicates the gravitational trajectory of the injected boron powder from IPD ($R = 1.57$ m). (Right) Schematic illustrating the toroidal distribution of the IPD, diagnostics, and main heating systems. *Bt, Ip*, and visible CCD viewing directions are labelled.

the deuterium recycling coefficient (R) at the inner and outer divertor targets was scanned from a reference value of 0.98 down to 0.6, while recycling at other wall segments (excluding pumping surfaces) was set to unity. Neutral boron atoms were introduced as a volumetric source with an initial energy equivalent to a downward velocity of ~ 9 m s^{-1}.

Toroidal non-uniformity arising from a localized solid impurity source is a known concern, as impurities ionized on open field lines can be guided along flux tubes, potentially producing striation-like footprints. Three-dimensional (3D) modeling (EMC3-EIRENE) has shown toroidal modulation for localized injections in devices like DIII-D, EAST, and LHD [48–50]. Although the powder injection is spatially localized, the use of a 2D model assuming toroidal symmetry is justified by cross-field mixing and migration (erosion and redeposition), which distribute impurities toroidally on timescales significantly shorter than the injection duration (several seconds). This assumption is consistent with the experimental observation of a toroidally symmetric divertor response (see section 3.3). Furthermore, to address uncertainties regarding the precise particle ablation depth, a sensitivity analysis was conducted by varying the source location across the PFR, the inner SOL, and the pedestal foot region (labelled in the left panel of figure 1), ensuring the robustness of the physics conclusions.

3. Results

The experiments investigated the plasma response to boron powder injection in USN H-mode plasmas with identical major parameters (plasma current $Ip = 500$ kA, toroidal field $|Bt| = 2.5$ T, safety factor $q_{95} \approx 5.4$) but opposite toroidal field directions. We compare 'favorable *Bt*', where the ion grad-*B* drift is directed towards the upper X-point (relevant for USN with counter-clockwise plasma current viewed from above), and 'unfavorable *Bt*', where the ion grad-*B* drift is directed away from the upper X-point. Boron powder was injected above the upper X-point into the PFR in both cases, with the same direction of the plasma current.

3.1. Favorable Bt direction

Under the favorable *Bt* configuration, boron powder injection facilitated the achievement of integrated ELM suppression and complete inner target detachment while maintaining or improving global plasma energy confinement. Figure 2 illustrates the time evolution of key plasma parameters for a typical discharge with boron injection (#85043) compared to a reference discharge without injection (#85041), both in favorable *Bt*. The boron powder was injected into the PFR above the upper X-point at a flow rate of approximately 10^{21} atoms s^{-1}, corresponding to $\sim$20 mg s^{-1}. Figure 2(a) shows the *B–V* emission intensity (a proxy for boron density) rising shortly after $t \sim 4.1$ s in discharge #85043, indicating the onset of boron injection. Figure 2(b) displays the Dα emission evolution, which clearly shows large, repetitive bursts characteristic of Type-I ELMs in the reference discharge #85041 (blue line). In discharge #85043 (orange line), the ELMs are gradually suppressed starting around 4.9 s, coinciding with the increasing *B–V* signal. Concurrently with ELM suppression, significant changes were observed in the divertor conditions. Figures 2(j) and (k) show the electron temperature on the upper inner target (Te_UI), measured by LPs in SOL near the strike point and PFR. In discharge #85043 (orange line), Te_UI drops dramatically from approximately 20 eV before injection to below 5 eV after $t \sim 6$ s, indicating inner divertor energy detachment. This detachment is further confirmed

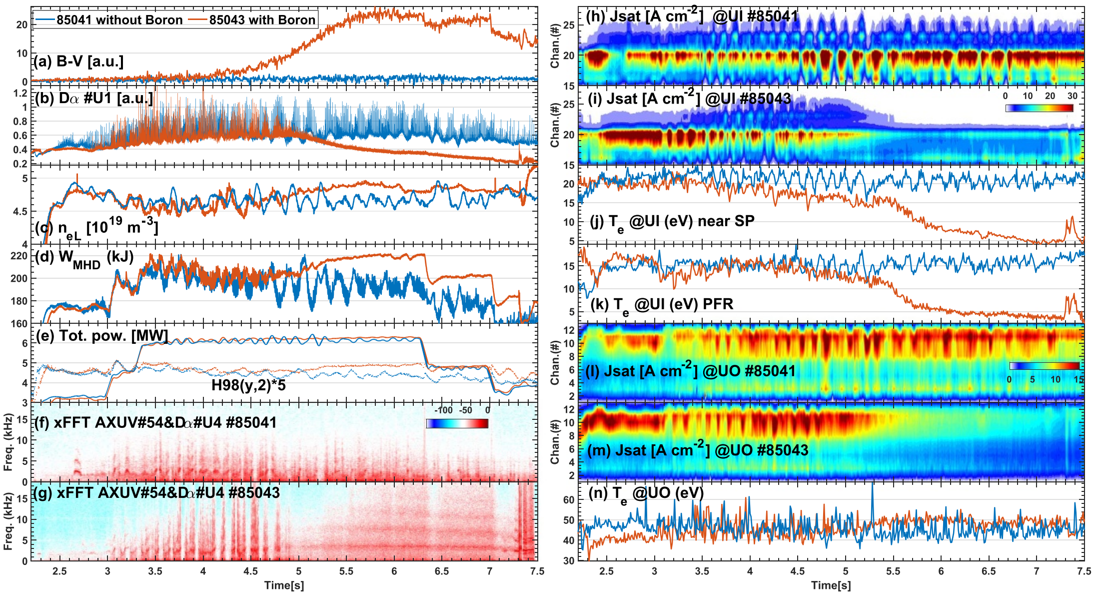

Figure 2. Time evolution of the experimental parameters for reference discharge #85041 (blue) and discharge #85043 (orange) with B powder injection ∼20 mg s^{-1}, Ip = 500 kA, central line-averaged density ∼4.5 × 10^{19} m^{-3}, favorable Bt = 2.5 T, $H_{98(y,2)}$ ∼ 0.95, total heating power ∼6 MW. (*a*) B–V emission, (*b*) Dα emission at the upper divertor, (*c*) line-averaged electron density, (*d*) stored energy, (*e*) $H_{98(y,2)}$ factor and total heating power including co-current NBI ∼ 2.8 MW, LHW ∼ 3 MW, and ECH ∼ 0.4 MW, (*f*), (*g*) cross-power spectrograms of AXUV #54 and Dα #U4 for #85041 and #85043. The right column shows divertor conditions: (*h*), (*i*) J_{sat} contour plots at the upper inner target, (*j*), (*k*) target T_e near the inner target strike point and private flux region, (*l*), (*m*) J_{sat} contour plots at the upper outer target, and (*n*) target T_e near the outer target strike point.

by the strong reduction and broadening of the ion saturation current (Js_UI) profile at the inner target, as shown in the contour plots comparing the reference case (figure 2(*h*)) and the boron-seeded case (figure 2(*i*)). In contrast, the outer target responded differently. Figure 2(*n*) shows the electron temperature on the upper outer target (Te_UO). Te_UO in discharge #85043 (orange line) remained high, between 40–50 eV, similar to the reference discharge #85041 (blue line). This demonstrates a strong in–out asymmetry in divertor detachment, with only the inner target detaching under favorable *Bt*. The impact on global plasma parameters was positive. Figure 2(*d*) shows the plasma stored energy (W_{MHD}). In discharge #85043, W_{MHD} increased by approximately 5%–10% during the ELM-suppressed phase compared to the phase before Boron injection in the same discharge and also relative to the reference discharge #85041. Figure 2(*c*) shows the line-averaged electron density (n_{eL}), which increased slightly during boron injection with feedback gas fueling reduction.

The suppression of ELMs was accompanied by the excitation of an Edge Harmonic Mode (EHM), consistent with previous observations [25–27]. Figures 2(*f*) and (*g*) show the cross-power spectrogram of signals from an AXUV channel (Ch 54) viewing the upper divertor/SOL and a Dα channel viewing the upper divertor. In contrast to the broadband ELM activity in the reference spectrogram (figure 2(*f*)), the spectrogram for the ELM-suppressed discharge #85043 exhibits a clear, coherent, fundamental mode and 2–3 harmonics (figure 2(*g*)). This EHM persisted during the ELM-suppressed phase and is often associated with benign edge stability and improved confinement in H-mode plasmas.

3.2. Unfavorable Bt direction

The plasma response to boron powder injection was significantly different when the toroidal field direction was reversed (plasma current was kept), resulting in the ion grad-*B* drift pointing away from the upper X-point (unfavorable *Bt*). Figure 3 shows the time evolution of parameters for a discharge with boron injection (#93469) and a reference discharge without injection (#93468) under unfavorable *Bt*. The boron injection rate in #93469 was comparable to #85043 in the favorable *Bt* case (∼20 mg s^{-1}, indicated by the *B*–*V* signal rise in figure 3(*a*)).

Similar to the favorable *Bt* case, boron injection in #93469 led to effective ELM suppression, as seen in the disappearance of Dα bursts (figure 3(*b*)). This is also clearly visible in the cross-power spectrogram of a MP signal and a LP signal, where the broadband turbulence associated with ELMs in the reference discharge #93468 (figure 3(*f*)) is replaced by a coherent mode in the ELM-suppressed phase of #93469. However, the impact on confinement and divertor detachment differed notably. Figure 3(*d*) shows that W_{MHD} tended to be maintained or slightly decreased by about 3%–10% during the ELM-suppressed phase compared to the reference discharge. The line-averaged density (figure 3(*c*)) was kept at a later phase, rather than increased in the favorable

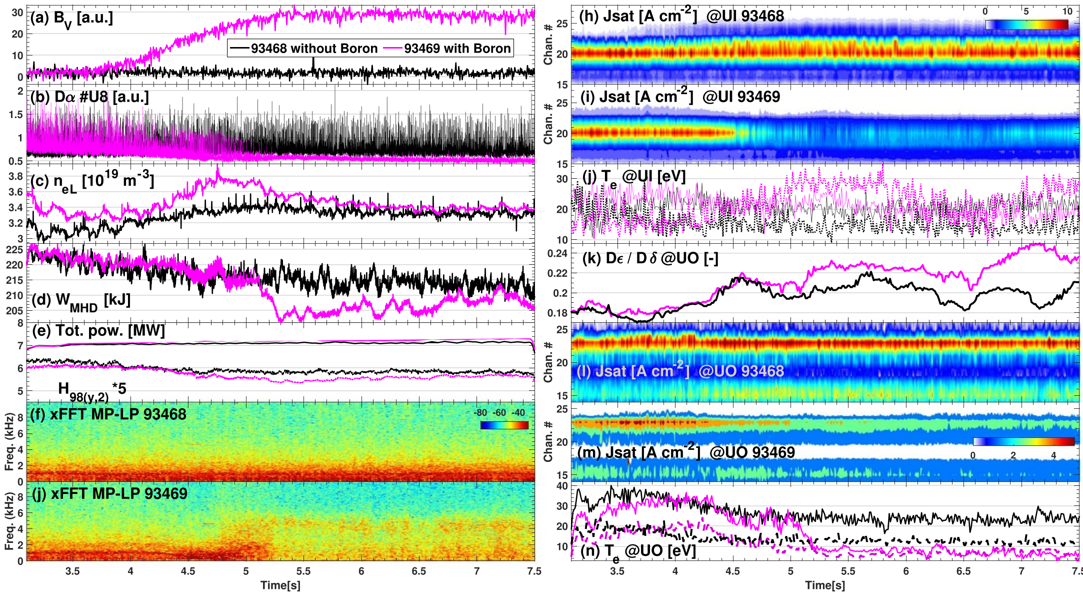

Figure 3. Time evolution of the experimental parameters for reference discharge #93468 (black) and discharge #93469 (magenta) with B powder injection ∼20 mg s^{-1}, Ip = 500 kA, central line-averaged density ∼3.2×10^{19} m^{-3}, unfavorable Bt = 2.5 T, $H_{98(y,2)}$ ∼ 1.2, total heating power ∼ 7.3 MW. (*a*) B–V emission, (*b*) Dα emission at the upper divertor, (*c*) line-averaged electron density, (*d*) stored energy, (*e*) $H_{98(y,2)}$ and total heating power including co-current NBI ∼ 3.9 MW, LHW ∼ 2.5 MW, and ECH ∼ 0.9 MW, (*f*), (*g*) cross-power spectrograms of a Mirnov probe (#1, midplane, HFS) and a Langmuir probe (UO#9) for #93468 and #93469. The right column shows divertor conditions: (*h*), (*i*) J_{sat} contour plots at the upper inner target, (*j*) target T_e from two LPs at the inner target, (*k*) ratio of D-epsilon to D-delta, measured by the outer target spectroscopy, (*l*), (*m*) J_{sat} contour plots at the upper outer target, and (*n*) target T_e from two LPs near the outer strike point.

Bt case, despite comparable boron injection rates, suggesting less favorable particle confinement, compared to the favorable *Bt* configuration, which is beneficial for impurity particle outward transport.

Regarding divertor conditions, improved power exhaust was observed in the outer divertor. Figure 3(*n*) shows Te_UO, measured by two LPs near the strike point, was significantly reduced from ∼25–40 eV to below 10 eV. Divertor spectroscopy measurements corroborate this temperature drop. Figure 3(*k*) shows the intensity ratio of two deuterium Balmer lines (Dε, $n = 7 \rightarrow 2$ at 396.9 nm to Dδ, $n = 6 \rightarrow 2$, at 410.06 nm), measured by visible spectroscopy viewing the outer target. This ratio is sensitive to the electron temperature in the recombination-dominated regime below ∼5 eV; an increase in the Dε/Dδ ratio indicates a reduction in the population of higher energy atomic levels, which is a signature of a cooling, recombining plasma [51, 52]. The rise of the Dε/Dδ ratio is consistent with the Te_UO drop. This transition towards detachment is also reflected in the ion saturation current at the outer target (Js_UO), which drops significantly (figure 3(*m*)) compared to the attached state in the reference shot (figure 3(*l*)). While not complete detachment of the outer target across its entire width, this represents a substantial reduction in heat and particle flux, indicating a transition towards a detached or strongly partially detached state for the outer divertor. On the other hand, the upper inner target electron temperature (Te_UI) does not drop clearly: rising slightly for some channels in SOL and dropping somewhat in the PFR.

Interestingly, while the inner target remained attached, the ion saturation current at the inner target (Js_UI) still showed a noticeable reduction, as seen by comparing the peak values in figures 3(*i*) and (*h*). The primary cause is the change in D recycling. Boron deposition on the divertor targets and surrounding surfaces acts as a getter for deuterium, significantly reducing the D recycling coefficient. This reduction in the neutral particle source from the target surface directly lowers the local plasma density and, consequently, the ion flux returning to the plate. Note that the gas puff for both discharges is the same. Similarly, in the favorable *Bt* case, while the outer target remained attached, the ion saturation current at the outer target (Js_UO) also showed a noticeable reduction, as seen by comparing the peak values in figures 2(*l*) and (*m*).

The fluctuations associated with ELM suppression also differed. Figure 3(*j*) shows the cross-power spectrogram for #93469. Instead of the EHM observed with favorable *Bt*, a distinct coherent mode at approximately 5 kHz was triggered and sustained during the ELM-suppressed phase. Compared to the EHM, this mode appeared as a single, dominant frequency without clear harmonics in the divertor viewing channels.

3.3. Toroidal symmetry and impact on wall conditioning and core-edge integration

A critical prerequisite for interpreting the localized powder injection experiments is establishing whether the plasma response is toroidally uniform. Figure 4 presents a direct comparison of signals from diagnostics located at widely separated toroidal sectors. Panels (*a*) and (*h*) display the B-II (visible, upper outer divertor) and *B–V* (EUV, midplane) emission intensities, which are separated by approximately 180°

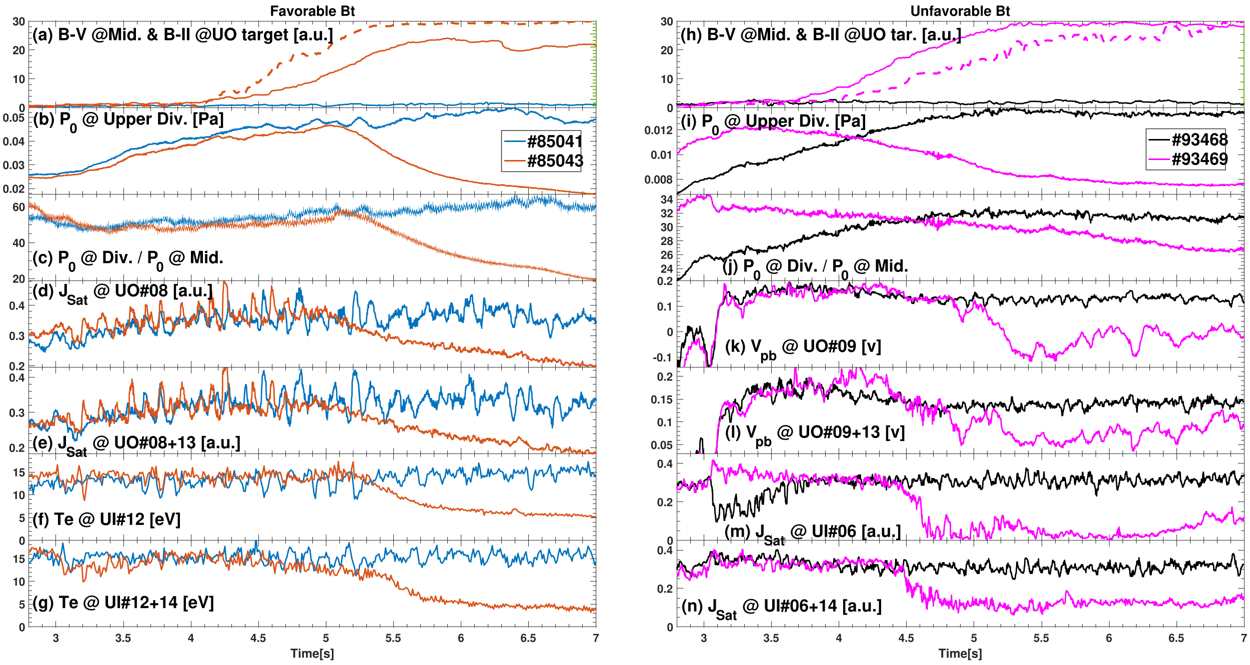

Figure 4. Experimental evidence for toroidal symmetry and neutral pressure evolution during boron powder injection: (Left column, (*a*)–(*g*)) Favorable *Bt* comparison; (Right column, (*h*)–(*n*)) Unfavorable *Bt* comparison. Panels ((*a*), (*h*)) show the simultaneous evolution of B-II emission (dashed line) and *B–V* emission (solid line). (*b*), (*i*) Divertor neutral pressure ($P_{0,\mathrm{Div}}$) measured behind the upper divertor dome. (*c*), (*j*) Divertor compression ratio, defined as the ratio of divertor pressure ($P_{0,\mathrm{Div}}$) to midplane pressure $P_{0,\mathrm{mid}}$). Panels ((*d*)–(g)) and ((*k*)–(*n*)) present ion saturation current (J_{sat}), electron temperature (T_{e}), and positive-bias potential (V_{pb}) signals from two identical upper divertor Langmuir probe arrays (Port D vs. Port O) separated by 135° toroidally. In the favorable *Bt* case, the J_{sat} drop at the upper outer target (UOLP#08 vs UOLP#21) and the T_{e} decrease in the inner PFR (UILP#12 vs UILP#26) occur simultaneously and with comparable magnitude in both arrays. Similarly, in the unfavorable *Bt* case, signals near the upper outer strike point (UOLP#09 vs UOLP#22) and inner strike point (UILP#06 vs UILP#20) evolve in similar trends.

toroidally. For both favorable and unfavorable *Bt* configurations, these signals rise and evolve simultaneously without significant phase delays or amplitude disparities. This is further corroborated by divertor conditions measured by two identical LP arrays separated by 135° (comparing Port D and Port O). As seen in figures 4(*d*)–(*g*) and (*k*)–(*n*), the reduction in J_{sat}, the drop in T_{e}, and the evolution of positive-bias potential (V_{pb}) occur symmetrically at both toroidal locations. The V_{pb} can be used to calculate the target T_{e} by the equation: $T_{\mathrm{e}} = (V_{\mathrm{pb}} - V_{\mathrm{f}}) / \ln 2$, where V_{f} is the floating potential measured by one of the triple tips left floating.

A plausible physical explanation for this near-toroidal symmetry is the combination of rapid parallel transport, $E \times B$ and ∇B drifts, turbulence mixing, and cycles of repeated ionization, wall-strike, and re-emission. The timescale to reach a stationary state with a relatively uniform wall coating and impurity density is estimated to be around 1 s, significantly shorter than the long injection duration of several seconds. If ionization occurs inside the last closed flux surface (LCFS), high parallel transport rapidly distributes impurity ions uniformly in the flux surface. If ionization occurs in the SOL, impurities are transported along open field lines to both divertor legs, with additional toroidal and poloidal spreading due to edge turbulence and drifts. This interpretation is supported by full-torus EMC3-EIRENE + DIS + WallDYN3D modeling of boron powder injection in related regimes, which suggests that while the early impurity plume is 3D, drifts and recycling smear out the toroidal distribution over tens to hundreds of milliseconds [22]. Crucially, a detailed analysis of the signal timing supports the hypothesis. In the favorable *Bt* case (#85043), the boron emission signals begin to rise at $t \approx 4.1$ s. However, the significant physical changes—ELM suppression, the reduction in neutral pressure ($P_{0,\mathrm{Div}}$), and the drop in target T_{e} and J_{sat}—all start almost simultaneously at a later time, $t \approx 4.9$ s. This delay (~ 0.8 s) indicates the timescale required for boron accumulation and redistribution to modify the wall condition, ELM activity, and detachment. Similarly, for the unfavorable *Bt* case (#93469), the time delay, ∼1–1.3 s, is similar to that of the favorable *Bt*.

This cumulative wall-conditioning effect manifests as a distinguishing feature of the boron-induced detachment: it occurs concomitant with a significant reduction in divertor neutral pressure ($P_{0,\mathrm{Div}}$) and compression ratio, as shown in figures 4((*b*), (*c*), (*i*) and (*j*)). This behavior indicates that detachment is driven primarily by impurity radiative cooling ('power starvation') while fresh boron layers actively pump deuterium, rather than by high neutral-pressure cushioning as in conventional gas-puff-induced detachment. We also observe a legacy effect: the pre-injection pressure (s) in #93469 is higher than in the reference #93468, likely due to the latency of boron deposited during the preceding discharge (#93467), which altered the initial wall state.

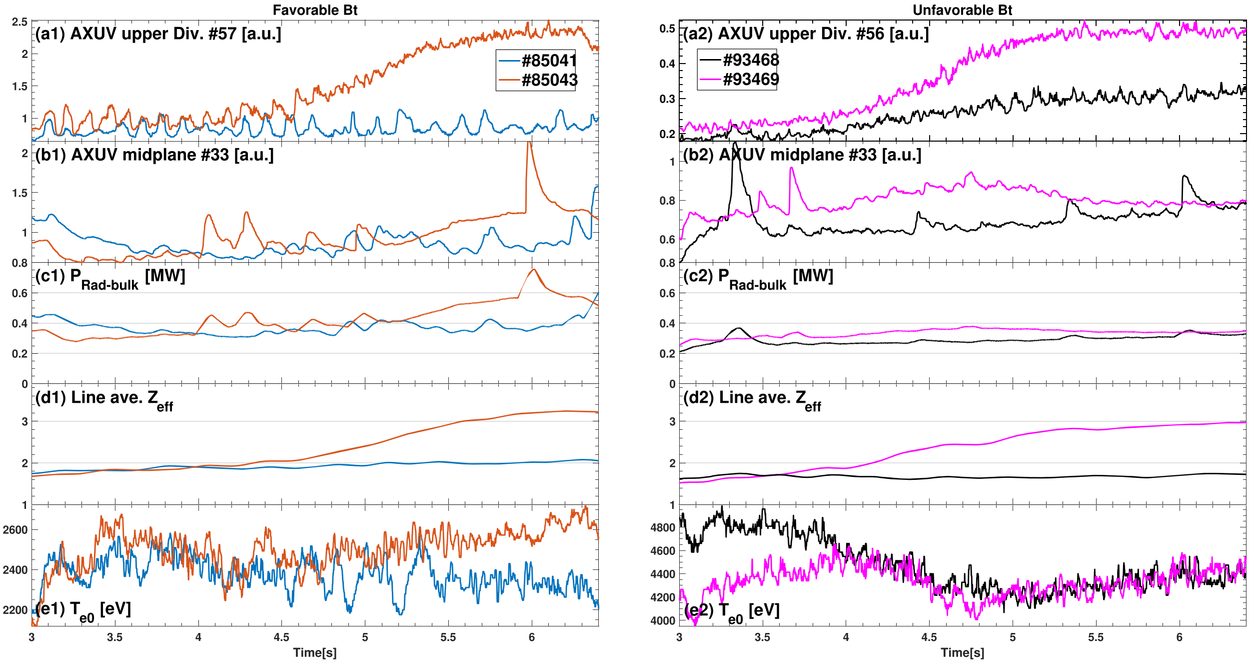

Figure 5. Evolution of radiated power, Z_{eff}, and T_{e0} for (Left column) Favorable *Bt* and (Right column) Unfavorable *Bt*. ((a)–(c)) Comparison of upper divertor radiation versus core-chord radiation (AXUV Ch#33) and total radiated power of bulk-plasma (excluding partial divertor radiation), showing that the radiation increase is dominated by the edge/divertor. (*d*) Line-averaged Z_{eff} derived from visible bremsstrahlung. (*e*) Core electron temperature (T_{e0}), showing that core confinement is maintained (favorable *Bt*) or slightly degraded (unfavorable *Bt*) during the injection.

This reduction in neutral pressure provides the key physical explanation for the behavior of the ion saturation current (J_{sat}) on the attached divertor legs (e.g. the outer target in favorable *Bt*). As shown in figures 4((*d*), (*e*), (*m*) and (*n*)), J_{sat} decreases even though the electron temperature remains high ($T_{\text{e}} > 10$ eV), ruling out the momentum loss by the volumetric recombination and charge exchange. Instead, the simultaneous drop in neutral pressure and J_{sat} indicates that the flux reduction is driven by the reduced ionization source resulting from the boron gettering effect. This is qualitatively supported by SOLPS-ITER simulations, where scanning the recycling coefficient *R* from 0.98 down to 0.6 reproduced the monotonic decrease in ion flux observed experimentally. These results are consistent with the experimental observations of lithium powder injection and associated SOLPS simulation on EAST [53].

The impact of this injection on core-edge integration is summarized in figure 5. The line-averaged effective charge (Z_{eff}), derived from line-integrated visible bremsstrahlung, is observed to increase by approximately 70% in favorable *Bt* and 100% in unfavorable *Bt* (figure 5(*d*)). However, it is important to note that this measurement likely overestimates the actual core fuel dilution, as the line-of-sight integration includes significant contributions from the boron-rich edge and SOL regions. This interpretation is supported by our SOLPS-ITER simulations, which indicate that Z_{eff} declines significantly from the outer boundary towards the inner boundary of the computational domain, suggesting that the impurity enhancement is largely peripheral. Similarly, experiments on ASDEX-Upgrade have shown that boron ion density profiles in H-mode are typically flat or hollow rather than centrally peaked during boron powder injection or boron source modulation [54, 55]. Consequently, despite the apparent rise in the line-integrated Z_{eff}, the core energy confinement is well preserved. The core electron temperature (T_{e0}) is maintained or even slightly increased during the injection phase (figure 5(*e*)). Crucially, the bolometry data (figures 5(*a*)–(*c*)) reveals that the increase in total radiated power is dominated by the edge and divertor regions, with only a mild rise in core radiation, confirming that boron powder injection successfully achieves a radiative divertor solution compatible with high core performance.

3.4. SOLPS-ITER simulations on the impact of E × B drifts

To understand the physical mechanisms underlying the observed impact of the toroidal field direction on divertor detachment asymmetry and impurity distribution, particularly the role of $E \times B$ drifts, qualitative comparisons were made with simulations performed using the SOLPS-ITER code suite [47, 56]. These simulations modeled the edge plasma and divertor regions, including the injection and transport of boron impurity, and incorporated the effects of $E \times B$ drifts [47]. Although the powder injection is spatially localized, the use of a 2D model assuming toroidal symmetry is justified by the experimental validation of a symmetric divertor response presented in section 3.3.

Figures 6(*a*) and (*b*) show the simulated electron temperature profiles along the inner and outer divertor targets ($T_{\text{e\_t}}$ vs R-Rsep, the distance from the strike point) for the favorable

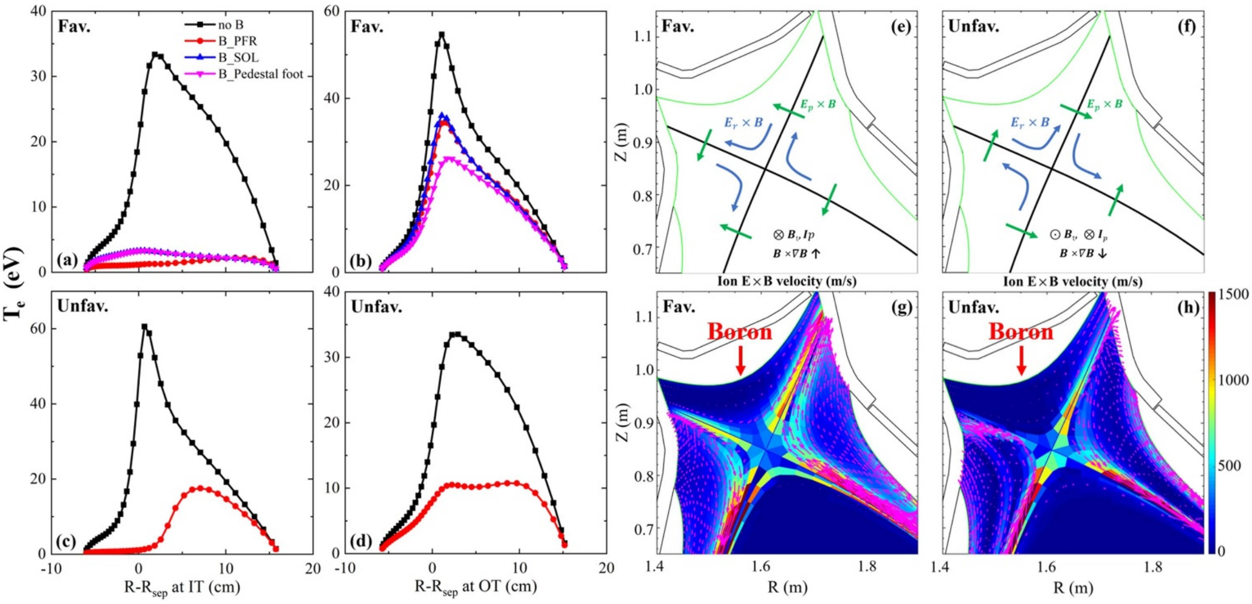

Figure 6. Results from qualitative SOLPS-ITER simulations illustrating the impact of E × B drifts on divertor detachment and impurity transport. Panels (*a*) and (*b*) show simulated target electron temperature (Te_t) profiles vs R-Rsep for the inner and outer divertors, comparing cases with and without boron injection in favorable Bt. Three grid cells were scanned to represent boron ablation locations. Panels (*c*) and (*d*) show similar profiles for unfavorable Bt. (*e*) and (*f*) Schematic illustrations indicating key E × B drift directions in the SOL and PFR for the respective Bt configurations relative to the plasma current (Ip) and Bt field. (*g*) and (*h*) Simulated 2D vector fields of boron ion velocity in the SOL and PFR from SOLPS-ITER for favorable (*e*) and unfavorable (*f*) Bt, highlighting the distinct, asymmetric impurity transport pathways driven by E × B drifts.

Bt case, comparing scenarios with and without boron injection. As observed experimentally, the simulations predict a significant drop in T_{e_t} on the inner target after boron injection (figure 6(*a*)), indicating plasma detachment. However, the outer target T_{e_t} (figure 6(*b*)) remains relatively high, consistent with the attached plasma in the experiment. Since the precise ablation profile of the powder is not directly measured, a sensitivity analysis was performed to ensure the robustness of the simulation results. We varied the boron source location across three physically plausible zones: in the PFR, in the inner SOL, and just inside the separatrix. The results demonstrate that the primary conclusion—that $E \times B$ drifts determine the direction of the in–out asymmetry—is robust regardless of the precise ablation location. While the absolute temperature values vary slightly with the source penetration depth (more boron ions from the confined region are transported into the outer divertor), the qualitative reversal of the asymmetry pattern is insensitive to the exact source location, confirming that the global drift pattern is the dominant factor. For the favorable *Bt* case (figures 6(*a*) and (*b*)), the simulations consistently predict a significant drop in T_{e_t} on the inner target after boron injection, indicating plasma detachment, while the outer target remains attached with relatively high temperatures.

Figures 6(*c*) and (*d*) show similar simulated T_{e_t} profiles for the unfavorable *Bt* case. In this configuration, boron injection leads to a substantial reduction in T_{e_t} on *both* the inner and outer targets (figures 6(*c*) and (*d*)). The cooling effect is more symmetric. The divertor in–out asymmetry is less pronounced than in the favorable *Bt* case. This qualitative agreement between the SOLPS simulations and the experimental measurements (figures 2 and 3) supports the model's representation of the underlying physics controlling divertor detachment.

The key physical mechanism explaining the observed *Bt* dependence is the distinct pattern of $E \times B$ drifts in the SOL and PFR for different *Bt* directions. Panels (*e*) and (*f*) schematically illustrate the dominant $E \times B$ drift directions. The $E \times B$ drift velocity $\mathbf{v} = (\mathbf{E} \times \mathbf{B})/B^2$, where $\mathbf{E}$ is the electric field and $\mathbf{B}$ is the magnetic field. Under favorable *Bt*, the radial $E_\theta \times B$ drift in the outer SOL is directed radially inwards towards the separatrix/PFR. Once particles enter the PFR, the poloidal $Er \times B$ drift (driven by the radial electric field) tends to carry particles upwards along the field lines into the inner divertor region. This combined drift path effectively transports particles and injected impurities, like boron, from the outer SOL/PFR towards the inner divertor target. The simulated boron ion velocity fields shown in figure 6(*e*) for favorable *Bt* qualitatively confirm this asymmetric transport, showing a flow towards the inner divertor. This accumulation of boron and increased particle flux in the inner divertor enhances local radiation and cooling, promoting detachment of the inner target.

In contrast, under unfavorable *Bt*, the poloidal $Er \times B$ drift in the PFR is reversed. It tends to carry particles and impurities from the inner divertor region into the outer divertor region. The simulated boron ion velocity fields for unfavorable *Bt* in figure 6(*f*) show a different pattern, with more transport directed towards the outer divertor. This redistribution reduces the

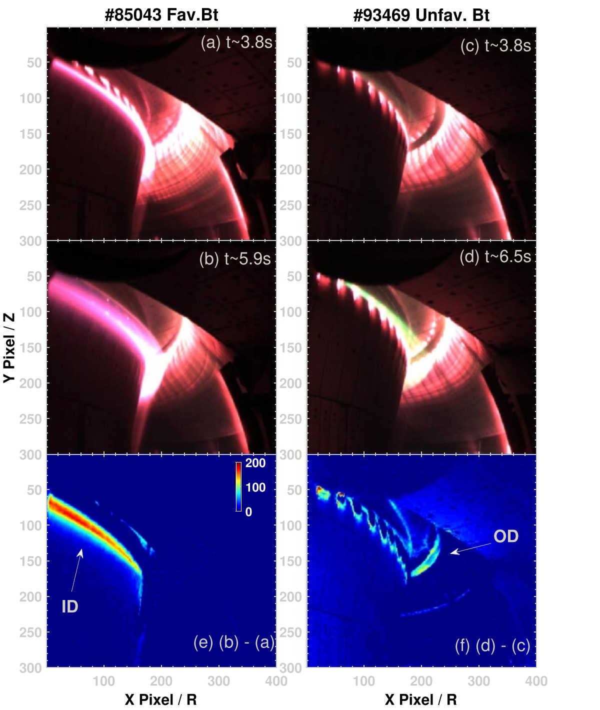

Figure 7. Visible CCD images with red, green, and blue components of the upper divertor region before and during boron powder injection for #85043 (Favorable Bt) and #93469 (Unfavorable Bt). (*a*) Image for #85043 at t = 3.8 s (before injection). (*b*) Image for #85043 at t = 5.9 s (during injection). (*c*) Image for #93469 at t = 3.1 s (before injection). (*d*) Image for #93469 at t = 6.5 s (during injection). (*e*) Differential image (panel (b)–panel (a)) of the blue component for #85043, highlighting the spatial distribution of boron-induced radiation in the inner divertor (ID). (*f*) Differential image (panel (*d*) minus panel (c)) of the blue component for #93469, highlighting the spatial distribution of boron-induced radiation in the outer divertor (OD).

effectiveness of boron in promoting inner detachment while enhancing its effect on the outer target. This shift in impurity and particle deposition due to the reversed $E \times B$ drift explains why the outer target detaches more readily under unfavorable *Bt* compared to favorable *Bt*, leading to a more symmetric divertor plasma state. The SOLPS-ITER simulations, by capturing these fundamental $E \times B$ drift effects, qualitatively reproduce the experimentally observed *Bt*-dependent in–out asymmetry in divertor detachment and highlight the critical role of drifts in controlling impurity transport pathways.

3.5. Experimental signature with differing E × B drift direction

Experimental data obtained from visible CCD imaging and AXUV array also show significant differences with differing *Bt* directions, which is consistent with the role of $E \times B$ drifts in steering injected impurities and causing the observed in–out asymmetry [28, 47]. As Boron radiates significantly in the visible spectrum, particularly in the blue range, the spatial distribution of blue light emission can indicate where the injected boron accumulates and radiates. Figure 7 shows visible CCD images of the upper divertor region for discharges #85043 (favorable *Bt*) and #93469 (unfavorable *Bt*) before and during boron injection. Figures 7(*a*) and (*c*) show images taken before injection, establishing baseline light distribution. Figures 7(*b*) and (*d*) show images during the steady phase of boron injection for favorable and unfavorable *Bt*, respectively. The dominant emission in divertor plasma from boron comes from singly ionized boron (B-II, 410–412 nm). This wavelength corresponds to the blue component of the RGB CCD camera. Dominated by D_α emission at 656.1 nm corresponds to the red component. When you mix the intense Red (D_α) with the strong Blue (boron), the human eye (and the composite RGB image) sees Purple/Magenta, as shown in figure 7(*b*). For isolating the boron contribution, the blue components were extracted from the camera original images, and differential images were obtained by subtracting the pre-injection image from the during-injection image for the blue color component (figures 7(*e*) and (*f*)).

The differential images reveal the spatial distribution of the additional blue radiation caused by boron. Under favorable *Bt* (figure 7(*e*), a clear belt of enhanced blue emission is observed in the **inner divertor region (ID)**, indicated by the bright area on the left side of the divertor leg. This confirms that boron preferentially radiates at the inner divertor. In contrast, under unfavorable *Bt* (figure 7(*f*), the enhanced blue emission is observed in the **outer divertor region (OD)**, indicated by the bright area on the right side. This experimental observation of the boron radiation enhancing the radiation at the outer target, even shifting from the inner to the outer divertor when the *Bt* direction is reversed, is consistent with SOLPS simulations that indicate $E \times B$ drifts are altering the injected boron and deuterium ions flows.

Further experimental support comes from the AXUV diode arrays, which measure line-integrated power profiles. By comparing the radiation profiles before and during boron injection for the two *Bt* directions, we can see how the spatial distribution of radiation changes. The left panel of figure 8 shows the ratio of the averaged AXUV signal during boron injection to the averaged signal before injection for chords viewing the upper divertor, plotted against the channel number. The right panel of figure 8 shows the viewing chords for these AXUV channels overlaid on the plasma equilibria for both discharges (note the slight difference in equilibrium position). Lower channel numbers correspond to chords viewing the inner divertor region, while higher channel numbers view the outer divertor region.

For the favorable *Bt* case (#85043, orange stars), the radiation ratio peaks around Channel 56, which corresponds to a view primarily focused on the inner divertor leg, consistent with the CCD images. For the unfavorable *Bt* case (#93469, magenta circles), the peak of the radiation ratio shifts outwards to channel 59, which is closer to the outer divertor region. The ratio in channels viewing the inner divertor region (e.g. channels 53–58) is generally lower in the unfavorable *Bt* case compared to the favorable *Bt* case, despite comparable boron injection rates. This spatial shift in the radiation peak from

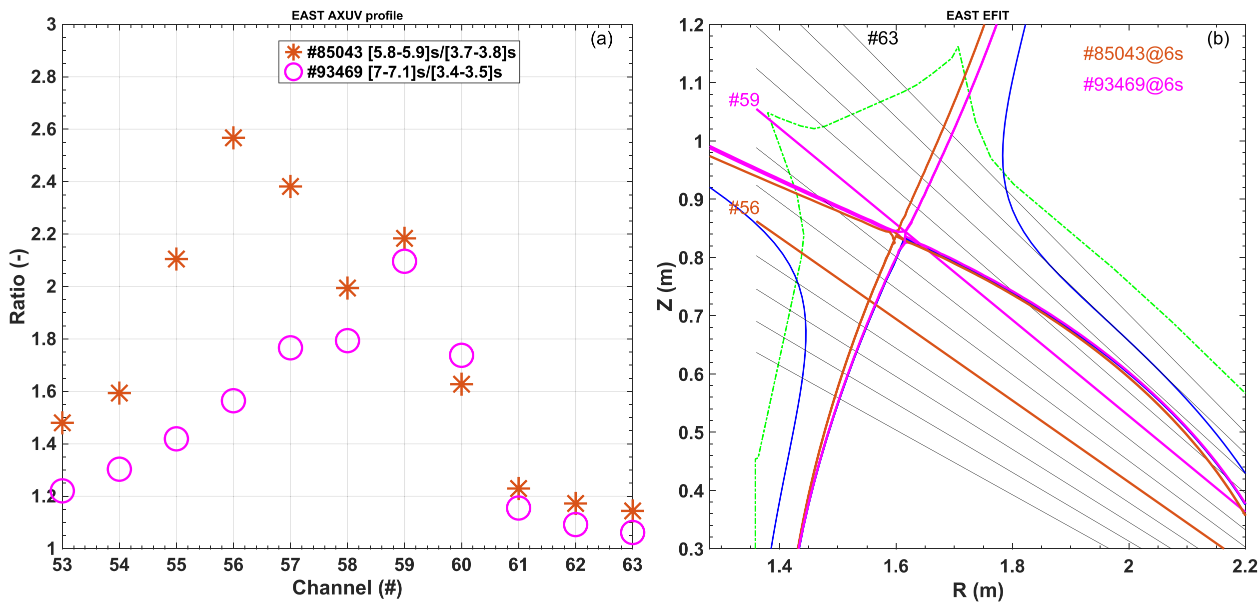

Figure 8. Experimental evidence for the spatial redistribution of radiation due to boron injection under different Bt directions, measured by the AXUV array viewing the upper divertor. Left panel: Radiation ratio profiles (Averaged AXUV signal during B injection/Averaged AXUV signal before B injection) versus AXUV channel number for #85043 (Favorable Bt, orange star) and #93469 (Unfavorable Bt, magenta circles). Smaller channel numbers view the inner divertor, while higher channels view the outer divertor. Right panel: AXUV viewing chords corresponding to the channels in the left panel, overlaid on the plasma equilibria for #85043 and #93469. The chords with the peak radiation ratio for each Bt direction (#56 for Fav Bt, #59 for Unfav Bt) are thickened to highlight the spatial shift.

the inner to the outer divertor as the *Bt* direction is reversed is consistent with the effect of $E \times B$ drifts on redistributing the particles and the injected boron, and the resulting radiated power.

3.6. Comparison of plasma response dependences on boron flow rate

The response of the plasma to boron powder injection, particularly regarding the operational window for ELM suppression and its impact on plasma performance, was found to be fundamentally different depending on the toroidal field direction. A series of experiments scanning the boron injection rate, monitored by the *B–V* emission signal, revealed a much wider and more robust operational space for maintaining high-confinement, ELM-stable scenarios in the favorable *Bt* configuration compared to the unfavorable *Bt* case. This section details these differences by analyzing the ELM suppression threshold, the operational limits, the wall conditioning effect, the resulting plasma performance, and the distinct low-frequency modes that were excited.

In both *Bt* directions, a clear threshold injection rate was required to transition the plasma from a state with regular or mitigated Type-I ELMs to a fully ELM-suppressed state. Figure 9 illustrates this transition for representative discharges. In the favorable *Bt* case, comparing discharges #93166 (lower rate) and #93165 (higher rate), a modest increase in the *B–V* signal was sufficient to achieve complete ELM suppression, as seen in the disappearance of ELM bursts on the Dα signal. Similarly, for the unfavorable *Bt* case, comparing #93467 (lower rate) and #93472 (higher rate) demonstrates a comparable threshold behavior. This indicates that a marginal flow rate is sufficient to access the ELM-suppressed regime regardless of the *Bt* direction.

However, the impact on plasma performance at this threshold was markedly different. For the favorable *Bt* discharges, crossing the ELM suppression threshold led to a beneficial plasma response. As seen when comparing discharges #93162 (pre-threshold), #93166 (at threshold), and #93167 (post-threshold), achieving ELM suppression was accompanied by a slight increase in both W_{MHD} and n_{eL}. For example, in discharge #85043 (figure 2), operating with a higher baseline density, ELM suppression resulted in a $\sim$10% increase in W_{MHD} and $\sim$5% in density, with T_{e0} remaining stable or slightly increasing initially. This suggests that in the favorable *Bt* case, ELM suppression is compatible with, and even conducive to, improved plasma confinement.

In stark contrast, for the unfavorable *Bt* configuration, achieving ELM suppression came at the cost of confinement. In the discharge pair #93467 and #93468 (reference), the plasma with a just-sub-threshold injection rate showed mitigated ELMs with W_{MHD} and density values comparable to the no-injection reference. However, upon crossing the threshold to achieve full suppression (e.g. #93472), W_{MHD} consistently decreased by up to 10%, while the core T_{e0} was maintained. This confinement degradation became more pronounced at higher injection rates, with W_{MHD} dropping by as much as 15% relative to the pre-injection phase, indicating a clear trade-off between ELM stability and energy confinement in this configuration.

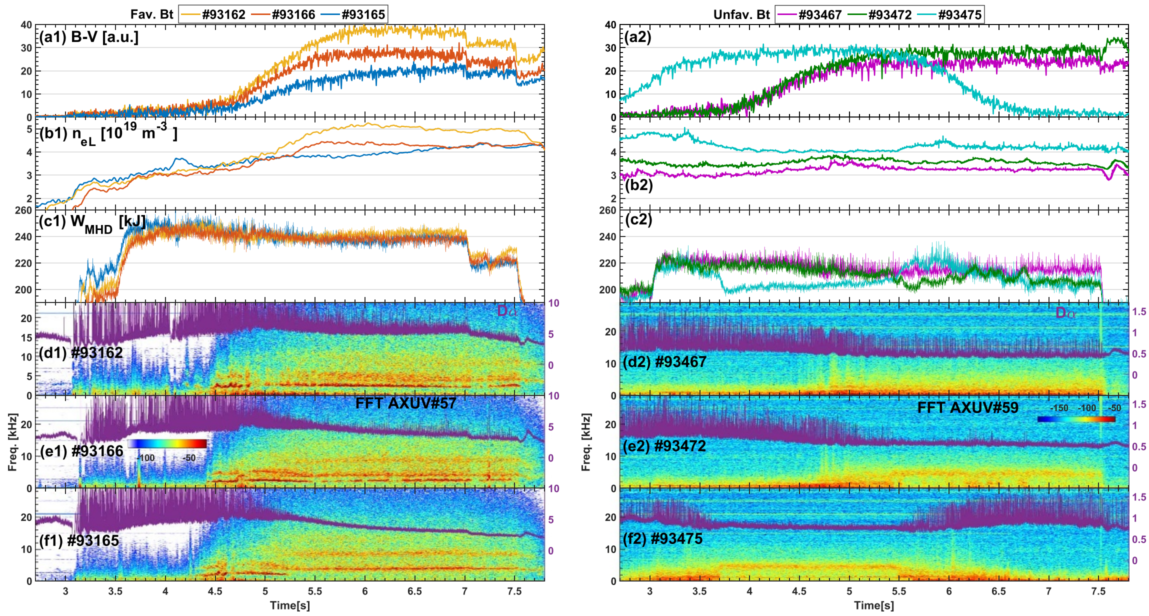

Figure 9. Time evolution of key parameters illustrating the ELM suppression threshold for favorable Bt (left panels, comparing #93162, #93166, and #93165) and unfavorable Bt (right panels, comparing #93467 and #93472, and #93475). Shown are: (a1), (a2) B–V emission, (b1), (b2) line-averaged electron density, (c1), (c2) plasma stored energy, and (d), (e), (*f*) FFT spectrograms of an AXUV signal (Ch 57 for favorable Bt, Ch 59 for unfavorable Bt) showing the transition from ELMy to ELM-suppressed states and the corresponding evolution of low-frequency modes as the injection rate increases and time shifts. The Dα emission from the upper divertor is overlaid.

The disparity between the two configurations became even more evident when exploring the upper limits of the boron injection rate to keep H-mode, as summarized in the multi-shot overview of figure 10. The favorable *Bt* scenario demonstrated a significantly larger operational window for sustaining H-mode. Discharges in this configuration could tolerate substantially higher boron injection rates before a disruptive event or a back-transition to L-mode occurred. For example, discharge #93163 (favorable *Bt*) was sustained in H-mode with a boron flow rate that was approximately 60%–80% higher than that of discharge #93465 (unfavorable *Bt*), which had a similar baseline density but lost H-mode due to the high impurity influx. This demonstrates a superior resilience to impurity seeding in the favorable *Bt* case.

The operational window for the unfavorable *Bt* case was not only narrower but also showed a dependency on the baseline plasma density. It was observed that increasing the electron density allowed the plasma to tolerate a slightly higher boron injection rate. For instance, discharge #93476, with a higher boron rate than #93465, successfully maintained H-mode until approximately $t = 5.5$ s, likely due to a higher baseline density. However, at higher injection rates, discharges in this configuration often terminated with a loss of H-mode, sometimes transitioning into I-mode characterized by a Weakly Coherent Mode (WCM), which warrants further study. This sensitivity suggests that the underlying transport and stability in the unfavorable *Bt* configuration are less robust against perturbations from impurity seeding.

The ELM-suppressed states in the two configurations were characterized by distinct low-frequency MHD modes. In the favorable *Bt* case, ELM suppression was consistently accompanied by the excitation of two EHMs. A ∼4 kHz EHM was identified as a global mode, observed across all poloidal MPs and in the lower AXUV channels (#7–10) that view the SOL and pedestal region. Its detection on the low-field side reflectometer confirmed its location within the steep pedestal gradient region. A second, more localized 2.5 kHz EHM with several harmonics was observed predominantly in diagnostics viewing the upper divertor region, including MPs, divertor LPs, and the upper Dα array. In discharge #93162 and #93166 with a marginal rate, both the 2.5 kHz and 4 kHz modes appeared and persisted to the H–L transition at ∼7.8 s. As the injection rate increased (e.g. discharge #93165, higher *B–V*), the ∼4 kHz mode became stronger than discharge #93162 and #93166, exhibiting clearer harmonics. The ∼2.5 kHz mode and the second harmonic emerged but did not persist. Previous work has shown that these EHMs enhance particle transport [25, 26, 57, 58], which is believed to be a key mechanism for maintaining a stationary, ELM-free H-mode by preventing excessive pedestal pressure buildup.

In the unfavorable *Bt* case, a coherent mode at approximately 5 kHz with a toroidal mode number of $n = 1$ was triggered upon ELM suppression. This mode was also global in nature, observed on all poloidal MPs and lower AXUV channels, but critically, it lacked the distinct harmonic structure of the EHM. When ELMs were still present but mitigated (e.g. in #93467 and #93472 around $t = 6.4$ s), this mode appeared as a broadband mode co-existing with the small/less ELMs. The fundamentally different nature of the instability-an EHM with multiple harmonics in the high-confinement,

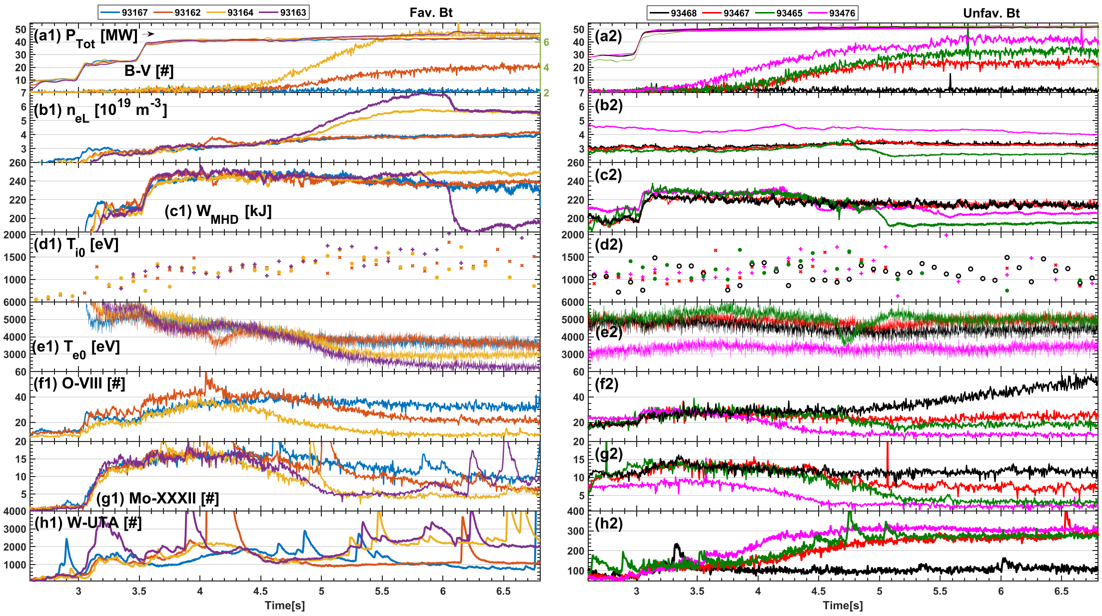

Figure 10. Comparison of plasma response during a boron flow rate scan for favorable Bt (left panels, four discharges) and unfavorable Bt (right panels, four discharges). Time traces are shown for: (a1), (a2) B–V emission (proxy for B rate) and total heating power; (b1), (b2) line-averaged electron density; (c1), (c2) plasma stored energy; (d1), (d2) core ion temperature; (e1), (e2) core electron temperature from ECE; (f1), (f2) O-VIII impurity line emission; (g1), (g2) Mo-XXXII impurity line emission; and (h1), (h2) core W-UTA emission. For #93163, B–V, O-VIII, and T_{i0} data are unavailable due to diagnostic issues. The flow rate of 93163 is about 50% higher than that of 93164, as indicated by the IPD flowmeter and the line density increase.

favorable *Bt* case versus a single $n = 1$ mode in the degraded-confinement, unfavorable *Bt* case-strongly suggests a link between the impurity dynamics (driven by $E \times B$ transport), changes in edge profiles (density, temperature), and plasma stability.

To consolidate the observations from the rate scan, figure 11 presents scatter plots of various plasma parameters as a ratio (value during boron injection phase divided by value before injection in the same discharge) plotted against the *B–V* emission from EUV (figure 11(*a*)), which serves as a consistent proxy for the boron injection flow rate across different discharges. The data points chosen for H-mode state distinguish between favorable *Bt* (circles) and unfavorable *Bt* (squares). This analysis confirms and quantifies the trends observed in the time traces.

Several **similarities** were observed in the plasma response to boron injection, regardless of the *Bt* direction:

- **Flowrate linearity:** Figure 11(*a*) plots the IPD flow meter signal (measured powder rate) against the *B–V* signal. The linear correlation confirms that the *B–V* signal is a reliable proxy for the injection rate across the scan, validating its use as the independent variable.
- **Wall conditioning:** Boron coating deposited on the inner wall and divertor surfaces during injection provides real-time wall conditioning. This typically leads to reduced recycling, improved density control, and gettering of other impurities, particularly O [14, 16–19, 24], which is beneficial for H-mode operation. Evidence for reduced carbon, oxygen, and Mo impurities (figures 11(*h*) and figures 10(*f*)–(*g*)) and changes in divertor neutral pressure (Gauge signal, figure 11(*c*)) consistent with wall conditioning were observed in both *Bt* directions.
- **Core radiation:** Figure 11(*f*) shows the AXUV signal from a chord viewing the midplane (Ch 33), representative of core radiation. Boron injection caused a mild/no increase in core radiation in both cases, but the increase was relatively small compared to the radiation changes in the divertor (figure 11(*e*)), suggesting that boron primarily radiates in the cooler edge/divertor and does not lead to significant core contamination at these injection rates. Note that the radiation power in the SOL and pedestal region can contribute to the core line-integrated radiation power measurement by AXUV#33, but not as much as the core radiation.

However, significant **differences** were observed depending on the toroidal field direction, particularly concerning plasma confinement, density behavior, and tungsten impurity levels:

- **Plasma confinement (W_{MHD}, n_{eL}):** As shown in figure 11(*b*), the plasma stored energy (W_{MHD}, ratio $\sim$1.1) tended to increase or be maintained at a higher level with boron injection in favorable *Bt*, as compared to the pre-injection phase. Figure 11(*d*) shows that the line-averaged density (n_{eL}, ratio > 1) consistently increased during boron injection, while the gas fueling is actually reduced by the feedback control. In general, the time evolution of n_{eL} reflects a balance between particle sources (external gas fueling, wall recycling, and ionization of injected impurities such as boron) and particle losses (transport to the wall and pumping), so an increase in n_{eL} can result from

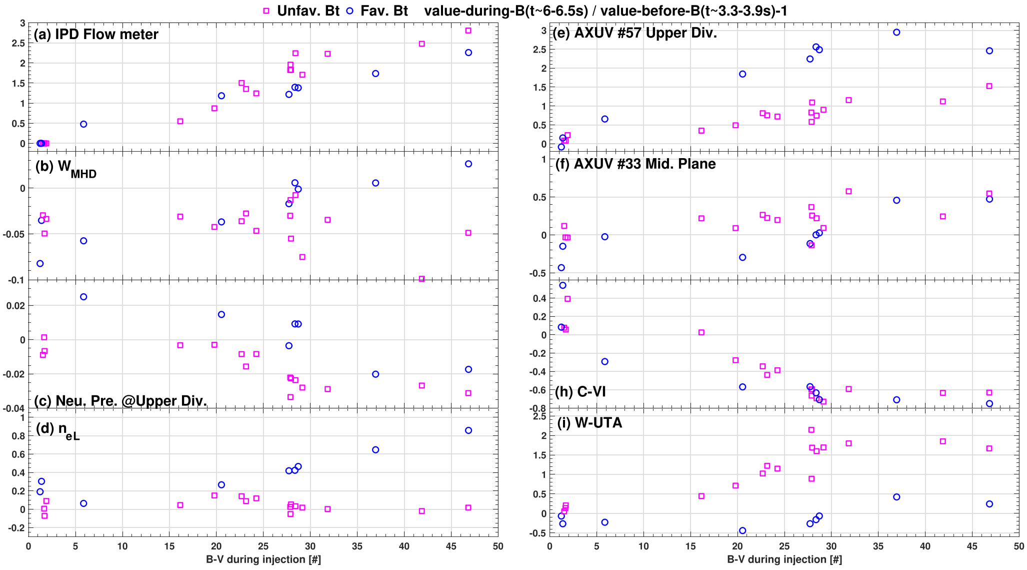

Figure 11. Comparative analysis of the response of various global and local plasma parameters to boron injection rate, represented by the B–V emission signal (proxy for rate). Data points are shown as ratios (averaged value during the Boron injection phase/averaged value before the injection phase − 1) to highlight the change caused by injection. Favorable Bt discharges are shown as blue circles, unfavorable Bt discharges as magenta squares. Plots show the ratio for: (*a*) flow meter measurement (validation of B–V as rate proxy). (*b*) Plasma stored energy (W_{MHD}). (*c*) Gauge signal from upper divertor (neutral pressure). (*d*) Line-averaged electron density (n_{eL}). (*e*) AXUV signal from upper divertor (Ch 57, favorable Bt; Ch 59, unfavorable Bt). (*f*) AXUV signal from midplane (Ch 33, core radiation). (*h*) C-VI signal (carbon impurity). (*i*) W-UTA signal (core tungsten impurity). This figure highlights similarities and differences in the plasma response between the two Bt directions as a function of injection rate.

either a stronger net source or improved particle confinement. At the same time, the upper-divertor neutral pressure decreases, consistent with real-time wall conditioning and reduced recycling due to boron deposition. This combination suggests improved particle confinement, while reduced recycling and boron-induced sources may influence the detailed density evolution but cannot alone explain the different n_{eL} trends between the two *Bt* directions. In our experiment, boron powder provides a comparable electron source for both *Bt* directions, so the observed difference in density trends reflects a difference in particle confinement, not source. In favorable *Bt*, n_{eL} increases with B injection, while in unfavorable *Bt*, it remains flat—indicating that particle confinement is improved only in favorable *Bt*. The increase in W_{MHD}/H_{98} and radiation power at nearly fixed heating power, together with the density rise, points to improved energy and particle confinement in favorable *Bt*.

- **Core tungsten (W-UTA):** Figure 11(*i*) shows the ratio of the W-UTA signal (core tungsten impurity emission). The change in the W-UTA signal with boron injection rate was comparatively lower in the favorable *Bt* case. This might indicate better core screening of tungsten impurities or a different transport behavior of tungsten due to the specific edge conditions established by boron injection under favorable *Bt*. A lower W-UTA increase is generally desirable for long-pulse operation. Figure 11(*i*) shows that under unfavorable *Bt*, the W-UTA signal ratio (increase relative to baseline) tended to be higher than in the favorable *Bt* case at comparable relative injection rates. This suggests potentially less effective core screening or different transport pathways for tungsten impurities from the divertor/SOL into the core under unfavorable *Bt*. However, it is noted that the absolute baseline W content in the unfavorable *Bt* discharges might have been lower than in the favorable *Bt* discharges (figure 10(*h*)), meaning the *absolute* W increase might not be strictly comparable across the ratio plot alone. Nonetheless, the higher *relative* increase could indicate a detrimental effect on W control for a given amount of injected boron. A potential reason for higher core W content could be increased sputtering from the outer target due to less effective detachment at the outer target compared to the inner target in favorable *Bt*, or increased leakage of W from the divertor/SOL into the core due to altered transport.
- **Edge/divertor radiation:** Figure 11(*e*) shows the AXUV signal from a channel viewing the upper divertor region (Ch 57), which traverses the inner divertor leg (figure 8 right). This signal shows a significant increase with Boron injection rate (up to 4× the background) under favorable *Bt*. This is consistent with the CCD observations (figure 7) and SOLPS predictions (figure 6), confirming that under favorable *Bt*, boron-induced radiation is strongly concentrated in the inner divertor. For unfavorable *Bt*, while there is an increase, the radiation redistribution indicated by CCD (figure 7) and AXUV profile (figure 8) suggests significant radiation also occurred in the outer divertor. The AXUV channel Ch 59 (figure 8) shows the peak shifting outwards, confirming that the radiation distribution is different, favoring the outer divertor more than in the favorable *Bt* case.

4. Discussion and conclusion

In summary, these experiments on EAST have demonstrated that boron powder injection is an effective technique for achieving integrated ELM suppression and enhanced divertor power exhaust, but its effectiveness and the resulting plasma state depend on the toroidal magnetic field direction. Under favorable *Bt*, boron injection enabled ELM suppression, complete inner divertor detachment, improved plasma confinement (increased W_{MHD} and n_{eL}), and the excitation of an EHM. Under unfavorable *Bt*, boron injection also suppressed ELMs and led to a more symmetric detachment state affecting both the inner and outer targets, but resulted in modestly reduced stored energy, accompanied by a low-frequency coherent mode that did not exhibit harmonics.

The contrasting divertor detachment asymmetry and impurity distribution observed experimentally with CCD and AXUV diagnostics are qualitatively consistent with SOLPS-ITER simulations incorporating $E \times B$ drifts. The underlying physical mechanism—the reversal of SOL/divertor particle and heat flux asymmetries with *Bt* direction—is a well-established phenomenon in tokamak physics [6]. The novelty of the present work is not in rediscovering this effect, but in demonstrating its critical and deciding role in the context of a modern, integrated plasma control scenario using real-time powder injection. Consistent with foundational $E \times B$ drift theory, our SOLPS-ITER simulations for boron injection show that drifts effectively channel particles and impurities towards the inner divertor in the favorable case and towards the outer divertor in the unfavorable case. This work provides the comprehensive experimental and modeling validation of these consequences for an integrated ELM-suppressed, detached-divertor scenario achieved with low-*Z* powder. This result confirms that drift physics is a primary factor in determining the efficacy and spatial distribution of power exhaust with impurity injection.

The observed differences in global plasma confinement and density behavior also align with and extend previous findings on EAST. In RF-heated H-modes without powder injection, the favorable *Bt* direction has been shown to generally yield better plasma performance than the unfavorable direction [59]. Our results demonstrate that this underlying performance difference persists and is amplified during impurity seeding: the favorable *Bt* drift pattern, which directs SOL flow towards the inner divertor, appears to establish edge profiles that are more conducive to improved particle and energy confinement. Conversely, the unfavorable *Bt* configuration, which led to degraded energy and particle confinement, tended to transition to an I-mode-like state at high injection rates. The characteristics of this state—an energy pedestal without a density pedestal—are similar to those observed with real-time lithium injection on EAST, which was also found to trigger I-mode [60]. The potential for boron powder to access this alternative confinement regime, and its implications for particle and impurity transport, represent a valuable topic for future investigation. The observed differences in core W accumulation also suggest varying effectiveness of impurity outward transport and screening depending on *Bt* direction and edge conditions. A higher increase in core W under unfavorable *Bt* could be related to reduced screening efficiency, increased W sputtering from the inner and outer targets (which detaches less readily than the inner target in favorable *Bt*), or enhanced impurity leakage from the SOL/PFR.

The distinct low-frequency modes observed (EHM under favorable *Bt*, coherent mode under unfavorable *Bt*) are likely a consequence of the different edge plasma profiles and stability properties established by the interplay of boron injection, radiation, detachment, and $E \times B$ transport in each *Bt* configuration. The EHM observed with favorable *Bt* is often associated with improved confinement and might contribute to the positive confinement sustainment in this scenario. The 5 kHz coherent mode observed under unfavorable *Bt* has different characteristics, and its relation to confinement is less clear from this study, though the scenario in which it appears shows degraded confinement. The underlying drive mechanisms for these modes require further investigation. Three hypotheses are being considered for the low-frequency modes: (1) being a type of Geodesic Acoustic Mode (GAM) driven by a density perturbation near the X-point [61], (2) driven by the negative temperature dependence of the radiated power [58], and (3) formed by the coupling of the rippling mode to the drift waves [57]. These mechanisms could be triggered or modified differently depending on the local profiles shaped by $E \times B$ transport and boron radiation.

Comparing these results to other impurity seeding experiments, boron powder injection in EAST shows similarities in achieving ELM suppression and detachment via increased radiation near the X-point or in the divertor legs, consistent with the 'X-point radiator' concept observed in LSN plasmas in other devices like AUG [62]. However, the strong dependence of the detachment asymmetry and confinement impact on the toroidal field direction, and the observation of different associated low-frequency modes (including the EHM) linked to these states, add new insights to the understanding of impurity transport and integrated edge control. The DIII-D observation of detachment-correlated modes with harmonics when the inner divertor detached while the outer remained attached [63] shares some qualitative similarities with the favorable *Bt* scenario here.

A distinguishing and physically significant feature of the boron-injection scenario observed in this study is the relationship between detachment and divertor neutral pressure. Unlike conventional gas-puff-induced detachment, which typically results in a high neutral density cushion to provide momentum dissipation (resulting in high divertor neutral pressure), the boron-induced detachment is observed concomitant with a significant reduction in divertor neutral pressure ($P_{0,\mathrm{Div}}$). This confirms that the detachment mechanism is primarily driven by impurity radiative cooling (power starvation), and that high neutral-pressure compression is not a necessary consequence. Simultaneously, the fresh boron layers deposited on the PFCs provide an active wall-conditioning (gettering) effect, reducing the recycling source, similar to the cropump in divertor. This 'low-pressure detachment' regime is particularly attractive for core-edge integration, as it achieves power exhaust while potentially minimizing the degradation of the H-mode pedestal collisionality typically associated with high neutral densities.

Assessing the extrapolability of these findings to ITER and future reactors requires a deeper understanding of the underlying physics, particularly the detailed interplay between $E \times B$ drifts, turbulent transport, impurity dynamics, and ELM stability across different magnetic configurations and divertor geometries. A real-time solid boron injector is being considered for ITER as a potential safeguard for tungsten source control [64], making these findings on drift-dependent transport and confinement highly relevant. ITER operates with a fixed *Bt* direction (favorable ion grad-*B* drift towards the lower X-point in LSN). The favorable *Bt* scenario in EAST (favorable drift towards the upper X-point in USN) is directly relevant for understanding the physics in the vicinity of the X-point and in the inner divertor of ITER, suggesting that boron powder injection might preferentially promote inner divertor detachment in ITER, similar to what is seen in EAST. The sensitivity of the operational window and confinement to *Bt* direction highlights the importance of accurately predicting and controlling impurity transport and edge profiles in future devices.

Further research is needed to confirm the proposed mechanisms for the observed low-frequency modes and their precise role in particle/energy transport and ELM suppression. More detailed edge profile measurements (T_e, n_e, flows) and specific impurity transport diagnostics are required to validate the SOLPS-ITER predictions quantitatively. Future experiments will provide valuable data to test the robustness of these findings and explore integrated scenarios under even more ITER-relevant conditions.

Acknowledgments

The authors would like to thank the EAST team for the support of the experiments, and gratefully acknowledge Huiqian Wang (GA), Laszlo Horvath (PPPL), Tao Zhang and Ran Chen (ASIPP), and Shahinul Islam (LLNL) for valuable discussions. This work was supported in part by the US Dept. of Energy contracts DE-AC02-09CH11466. This research was partly funded by the Strategic Priority Research Program of Chinese Academy of Sciences under Grant No. XDB0790102, the National Key Research and Development Program of China (2024YEF03000200, 2022YFE03180400, 2022YFE03040003, 2022YFE03010002, 2022YFE03100003, 2022YFE03130004, 2024YFE03020003, 2024YFE03250300), National Nature Science Foundation of China (12475208, 12475207, 12505266), Provincial Natural Science Foundation of Anhui (2408085J002, 2408085QA007), and Natural Science Foundation of Anhui Higher Education Institutions of China (2022AH050379). The United States Government retains a non-exclusive, paid-up, irrevocable, world-wide license to publish or reproduce the published form of this manuscript, or allow others to do so, for United States Government purposes. The data that support the findings of this study are available from the corresponding authors upon reasonable request. Raw data were generated at the EAST facility.

ORCID iDs

Zhen Sun 0000-0002-7224-3592
Rajesh Maingi 0000-0003-1238-8121
Xin Lin 0000-0003-4540-3017
Wei Xu 0000-0001-8619-6953
Zhe Wang 0009-0007-6857-1431
Qingquan Yang 0000-0002-6354-1408
Kaifu Gan 0000-0002-7207-3802
Ahmed Diallo 0000-0002-0706-060X
Yifeng Wang 0000-0002-0368-9566
Liang Chen 0000-0002-7176-4978
Kaixuan Ye 0000-0003-0927-4502
Wei Wang 0009-0007-6479-6326
Yunxin Cheng 0000-0002-9195-2757
Lingyi Meng 0000-0002-8633-5383
Yifei Jin 0000-0002-3061-6709
Jizhong Sun 0000-0002-2862-1437
Alessandro Bortolon 0000-0002-0094-0209
Guizhong Zuo 0000-0002-4149-089X
Jinping Qian 0000-0002-2646-6509
Xianzu Gong 0000-0001-6886-6431
Jiansheng Hu 0000-0002-8252-0960

References

[1] Loarte A. *et al* 2014 Progress on the application of ELM control schemes to ITER scenarios from the non-active phase to DT operation *Nucl. Fusion* **54** 033007
[2] Pitts R.A., Loarte A., Wauters T., Dubrov M., Gribov Y., Köchl F., Pshenov A., Zhang Y., Artola J. and Bonnin X. 2025 Plasma-wall interaction impact of the ITER re-baseline *Nucl. Mater. Energy* **42** 101854
[3] Krieger K., Brezinsek S., Coenen J.W., Frerichs H., Kallenbach A., Leonard A.W., Loarer T., Ratynskaia S., Vianello N. and Asakura N. 2025 Scrape-off layer and divertor physics: chapter 5 of the special issue: on the path to tokamak burning plasma operation *Nucl. Fusion* **65** 043001
[4] Fenstermacher M.E., Baylor L.R., de la Luna E., Dunne M.G., Huijsmans G.T.A., Kirk A., Laggner F.M., Osborne T.H., Paz-Soldan C. and Saarelma S. 2025 Progress in pedestal and edge physics: chapter 3 of the special issue: on the path to tokamak burning plasma operation *Nucl. Fusion* **65** 053001
[5] Pütterich T., Fable E., Dux R., O'Mullane M., Neu R. and Siccinio M. 2019 Determination of the tolerable impurity concentrations in a fusion reactor using a consistent set of cooling factors *Nucl. Fusion* **59** 056013
[6] Leonard A.W. 2018 Plasma detachment in divertor tokamaks *Plasma Phys. Control. Fusion* **60** 044001
[7] Beurskens M.N.A. *et al* 2008 Pedestal and ELM response to impurity seeding in JET advanced scenario plasmas *Nucl. Fusion* **48** 095004
[8] Rapp J., Eich T., von Hellermann M., Herrmann A., Ingesson L.C., Jachmich S., Matthews G.F., Philipps V. and Saibene G. (Contributors to the EFDA-JET Work Programme) 2002 ELM mitigation by nitrogen seeding in the JET gas box divertor *Plasma Phys. Control. Fusion* **44** 639
[9] Giroud C., Carvalho I.S., Brezinsek S., Huber A., Keeling D., Mailloux J., Pitts R.A., Lerche E., Henriques R. and Hillesheim J. 2024 The core–edge integrated neon-seeded

scenario in deuterium–tritium at JET *Nucl. Fusion* **64** 106062
[10] Li K. *et al* 2023 Compatibility of large ELM control and stable partial detachment with neon/argon seeding in EAST *Nucl. Fusion* **63** 026025
[11] Kallenbach A. *et al* 2020 Developments towards an ELM-free pedestal radiative cooling scenario using noble gas seeding in ASDEX Upgrade *Nucl. Fusion* **61** 016002
[12] Glöggler S. *et al* 2019 Characterisation of highly radiating neon seeded plasmas in JET-ILW *Nucl. Fusion* **59** 126031
[13] Nespoli F. *et al* 2022 Observation of a reduced-turbulence regime with boron powder injection in a stellarator *Nat. Phys.* **18** 350
[14] Schamis H. *et al* 2025 Wall conditioning effects of boron powder injection in KSTAR with a tungsten divertor *Nucl. Fusion* **65** 086037
[15] Krieger K., Balden M., Bortolon A., Dux R., Griener M., Hegele K., Laggner F., Rohde V. and Wampler W.R. 2023 Wall conditioning effects and boron migration during boron powder injection in ASDEX Upgrade *Nucl. Mater. Energy* **34** 101374
[16] Lunsford R. *et al* 2022 Real-time wall conditioning and recycling modification utilizing boron and boron nitride powder injections into the large helical device *Nucl. Fusion* **62** 086021
[17] Bodner G. *et al* 2022 Initial results from boron powder injection experiments in WEST lower single null L-mode plasmas *Nucl. Fusion* **62** 086020
[18] Afonin K. *et al* 2024 Boron powder injection experiments in WEST with a fully actively cooled, ITER grade, tungsten divertor *Nucl. Mater. Energy* **40** 101724
[19] Effenberg F. *et al* 2022 Mitigation of plasma–wall interactions with low-Z powders in DIII-D high confinement plasmas *Nucl. Fusion* **62** 106015
[20] Makarov S.O., Coster D.P., Gleiter T., Brida D., Muraca M., Dux R., David P., Kurzan B., Bonnin X. and O'Mullane M. 2024 First SOLPS-ITER simulations of ASDEX Upgrade partially detached H-mode with boron impurity: the missing radiation at the outer strike-point region *Contrib. Plasma Phys.* **64** e202300139
[21] Peng L., Sun Z., Sun J.-Z., Maingi R., Gao F., Bonnin X., Chang H.-Y., Wang W.-K. and Liu J.-Y. 2024 Comparative study of boron and neon injections on divertor heat fluxes using SOLPS-ITER simulations *Chin. Phys. B* **33** 115201
[22] Effenberg F., Schmid K., Nespoli F., Bortolon A., Feng Y., Grierson B.A., Lore J.D., Maingi R. and Rudakov D.L. 2025 Integrated modeling of boron powder injection for real-time plasma-facing component conditioning *Nucl. Mater. Energy* **42** 101832
[23] Sun Z. *et al* 2021 Type-I ELM mitigation by continuous lithium granule gravitational injection into the upper tungsten divertor in EAST *Nucl. Fusion* **61** 066022
[24] Gilson E.P. *et al* 2021 Wall conditioning and ELM mitigation with boron nitride powder injection in KSTAR *Nucl. Mater. Energy* **28** 101043
[25] Sun Z. *et al* 2021 Enhancement of edge turbulence concomitant with ELM suppression during boron powder injection in EAST *Phys. Plasmas* **28** 082512
[26] Sun Z. *et al* 2021 Suppression of edge localized modes with real-time boron injection using the tungsten divertor in EAST *Nucl. Fusion* **61** 014002
[27] Maingi R. *et al* 2020 ELM suppression by boron powder injection and comparison with lithium powder injection on EAST *J. Fusion Energy* **39** 429
[28] LaBombard B. *et al* 2004 Transport-driven scrape-off-layer flows and the boundary conditions imposed at the magnetic separatrix in a tokamak plasma *Nucl. Fusion* **44** 1047
[29] Casali L., Eldon D., McLean A., Osborne T., Leonard A., Grierson B. and Ren J. 2022 Impurity leakage and radiative cooling in the first nitrogen and neon seeding study in the closed DIII-D SAS configuration *Nucl. Fusion* **62** 026021
[30] Casali L., Osborne T.H., Grierson B.A., McLean A.G., Meier E.T., Ren J., Shafer M.W., Wang H. and Watkins J.G. 2020 Improved core-edge compatibility using impurity seeding in the small angle slot (SAS) divertor at DIII-D *Phys. Plasmas* **27** 062506
[31] Senichenkov I.Y., Kaveeva E.G., Sytova E.A., Rozhansky V.A., Voskoboynikov S.P., Veselova I.Y., Coster D.P., Bonnin X. and Reimold F. 2019 On mechanisms of impurity leakage and retention in the tokamak divertor *Plasma Phys. Control. Fusion* **61** 045013
[32] Rozhansky V., Molchanov P., Veselova I., Voskoboynikov S., Kirk A. and Coster D. 2012 Contribution of ExB drifts and parallel currents to divertor asymmetries *Nucl. Fusion* **52** 103017
[33] Jaervinen A.E. *et al* 2018 E x B flux driven detachment bifurcation in the DIII-D Tokamak *Phys. Rev. Lett.* **121** 075001
[34] Ma X., Wang H.Q., Guo H.Y., Stangeby P.C., Meier E.T., Shafer M.W. and Thomas D.M. 2021 First evidence of dominant influence of E × B drifts on plasma cooling in an advanced slot divertor for tokamak power exhaust *Nucl. Fusion* **61** 054002
[35] Reinke M.L. *et al* 2019 Radiative heat exhaust in Alcator C-Mod I-mode plasmas *Nucl. Fusion* **59** 046018
[36] Nelson A.O., Schmitz L., Paz-Soldan C., Thome K.E., Cote T.B., Leuthold N., Scotti F., Austin M.E., Hyatt A. and Osborne T. 2023 Robust avoidance of edge-localized modes alongside gradient formation in the negative triangularity tokamak edge *Phys. Rev. Lett.* **131** 195101
[37] Wang H.Q. *et al* 2020 First evidence of local ExB drift in the divertor influencing the structure and stability of confined plasma near the edge of fusion devices *Phys. Rev. Lett.* **124** 195002
[38] Wang H.Q. *et al* 2018 Effects of divertor geometry on H-mode pedestal structure in attached and detached plasmas in the DIII-D tokamak *Nucl. Fusion* **58** 096014
[39] Menard J.E., Grierson B.A., Brown T., Rana C., Zhai Y., Poli F.M., Maingi R., Guttenfelder W. and Snyder P.B. 2022 Fusion pilot plant performance and the role of a sustained high power density tokamak *Nucl. Fusion* **62** 036026
[40] Wan B.N. *et al* 2022 Advances in the long-pulse steady-state high beta H-mode scenario with active controls of divertor heat and particle fluxes in EAST *Nucl. Fusion* **62** 042010
[41] Gong X. *et al* 2024 Overview of recent experimental results on the EAST Tokamak *Nucl. Fusion* **64** 112013
[42] Nagy A., Bortolon A., Mauzey D.M., Wolfe E., Gilson E.P., Lunsford R., Maingi R., Mansfield D.K., Nazikian R. and Roquemore A.L. 2018 A multi-species powder dropper for magnetic fusion applications *Rev. Sci. Instrum.* **89** 10K121
[43] Zhang L. *et al* 2015 A fast-time-response extreme ultraviolet spectrometer for measurement of impurity line emissions in the Experimental Advanced Superconducting Tokamak *Rev. Sci. Instrum.* **86** 123509
[44] Duan Y.M., Hu L.Q., Chen K.Y., Du W. and Zhang L. 2013 Radiation distribution and energy loss during ELM in EAST *J. Nucl. Mater.* **438** S338
[45] Xu J.C. *et al* 2018 Upgrade design of lower divertor Langmuir probe diagnostic system in the EAST Tokamak *IEEE Trans. Plasma Sci.* **46** 1331
[46] Mao H. *et al* 2017 A multichannel visible spectroscopy system for the ITER-like W divertor on EAST *Rev. Sci. Instrum.* **88** 043502
[47] Peng L. *et al* 2025 Role of E × B drift in divertor detachment control via boron powder injection on EAST *J. Fusion Energ.* **44** 9

[48] Effenberg F. *et al* 2021 3D modeling of boron transport in DIII-D L-mode wall conditioning experiments *Nucl. Mater. Energy* **26** 100900
[49] Wen Z.X., Gao G.D., Liu B., Chen Y.T., Liu L.Z. and Dai S.Y. 2023 Impacts of lithium injection positions on lithium transport and heat flux on EAST with EMC3-EIRENE modelling *J. Fusion Energy* **42** 39
[50] Shoji M. *et al* 2024 Full-torus impurity transport simulation in boron powder injection experiments in the large helical device *Nucl. Mater. Energy* **41** 101803
[51] Karhunen J., Lomanowski B., Solokha V., Aleiferis S., Carvalho P., Groth M., Kumpulainen H., Lawson K.D., Meigs A.G. and Shaw A. 2020 Estimation of 2D distributions of electron density and temperature in the JET divertor from tomographic reconstructions of deuterium Balmer line emission *Nucl. Mater. Energy* **25** 100831
[52] Park J.S., Groth M., Pitts R., Bak J.-G., Thatipamula S.G., Juhn J.-W., Hong S.-H. and Choe W. 2018 Atomic processes leading to asymmetric divertor detachment in KSTAR L-mode plasmas *Nucl. Fusion* **58** 126033
[53] Canik J.M. *et al* 2018 Active recycling control through lithium injection in EAST *IEEE Trans. Plasma Sci.* **46** 1081
[54] Bruhn C. *et al* 2020 Corrigendum: A novel method of studying the core boron transport at ASDEX Upgrade (2018 *Plasma Phys. and Control. Fusion* 60 085011) *Plasma Phys. Control. Fusion* **62** 049501
[55] Lunsford R. *et al* 2019 Active conditioning of ASDEX Upgrade tungsten plasma-facing components and discharge enhancement through boron and boron nitride particulate injection *Nucl. Fusion* **59** 126034
[56] Peng L., Sun J., Sun Z., Gao F., Bonnin X. and Liu J.Y. 2021 Numerical simulation study of impurity B transport during real-time B powder injection in EAST *Nucl. Mater. Energy* **26** 100937
[57] Ding G.F. *et al* 2023 Various edge low-frequency fluctuations during transition to a detached divertor in Experimental Advanced Superconducting Tokamak *Nucl. Fusion* **63** 066006
[58] Ye Y. *et al* 2021 Sustained edge-localized-modes suppression and radiative divertor with an impurity-driven instability in tokamak plasmas *Nucl. Fusion* **61** 116032
[59] Lin X. *et al* 2021 Plasma performance improvement with favourable Bt relative to unfavourable Bt in RF-heated H-mode plasmas in EAST *Nucl. Fusion* **61** 026014
[60] Zhong X.M. *et al* 2024 I-mode plasma confinement improvement by real-time lithium injection and its classification on EAST tokamak *Nucl. Fusion* **64** 126040
[61] Diallo A. *et al* 2021 First observation of ELM suppression without confinement degradation due to geodesic acoustic mode (GAM)-like mode triggered by boron powder injection *preprint 2020 IAEA Fusion Energy Conf. (Virtual Event 10–15 May 2021)* (available at: https://nucleus.iaea.org/sites/fusionportal/Shared%20Documents/FEC%202020/fec2020-synopsis/Synopsis1167.pdf)
[62] Bernert M. *et al* 2025 X-point radiation: from discovery to potential application in a future reactor *Nucl. Mater. Energy* **43** 101916
[63] Wang H.Q., Watkins J.G., Guo H.Y., Leonard A.W., Thomas D.M., Stepanenko A.A. and Krasheninnikov S.I. 2020 Enhanced particle flux due to localized divertor MHD instability in DIII-D tokamak *Phys. Plasmas* **27** 022504
[64] Snipes J.A. *et al* 2024 Initial design concepts for solid boron injection in ITER *Nucl. Mater. Energy* **41** 101809